



## Cobalt oxide nanoparticles on mesoporous MCM-41 and Al-MCM-41 by supercritical CO<sub>2</sub> deposition

Soledad G. Aspromonte<sup>a</sup>, Álvaro Sastre<sup>b</sup>, Alicia V. Boix<sup>a,\*</sup>, María J. Cocero<sup>b</sup>, Esther Alonso<sup>b</sup>

<sup>a</sup> Instituto de Investigaciones en Catálisis y Petroquímica, INCAPE (FIQ, UNL-CONICET), Santiago del Estero 2829, 3000 Santa Fe, Argentina

<sup>b</sup> High Pressure Processes Group, Chemical Engineering and Environmental Technology, University of Valladolid, C/Prado de la Magdalena s/n, 47011 Valladolid, Spain

### ARTICLE INFO

#### Article history:

Received 12 May 2011

Received in revised form 8 July 2011

Accepted 21 July 2011

Available online 29 July 2011

#### Keywords:

Supercritical CO<sub>2</sub>

Cobalt oxide nanoparticles

MCM-41

Al-MCM-41 and Mesoporous supports

### ABSTRACT

CoO and Co<sub>3</sub>O<sub>4</sub> nanoparticles were uniformly dispersed inside mesoporous MCM-41 and Al-MCM-41 supports using supercritical CO<sub>2</sub> reactive deposition. This method represents a one-pot reproducible procedure that allows the dissolution of the organocobalt precursor and supports impregnation in supercritical CO<sub>2</sub> at 70 °C and 110 bar, followed by the precursor thermal decomposition into cobalt species at 200 °C and 160 bar. By the relative concentration of the cobalt precursor [cobalt (II) bis (η<sup>5</sup>-cyclopentadienyl)], the load of cobalt nanoparticles was controlled and then determined by Inductively Coupled Plasma (ICP-OES). The synthesis of CoO and Co<sub>3</sub>O<sub>4</sub> species inside the MCM-41 and Al-MCM-41 substrates was confirmed by X-ray Photoelectron (XPS) and Laser Raman Spectroscopies (LRS). By N<sub>2</sub> adsorption and Small Angle X-ray Scattering (SAXS), it was determined that the hexagonal arrangement as well as the surface area and pore size of the substrates changed after the addition of cobalt. By means of X-ray mapping from SEM images, a homogeneous distribution of cobalt nanoparticles was observed inside the mesopores when the cobalt loading was 1 wt.%. In addition, spherical cobalt nanoparticles of average diameter close to 20 nm were detected on the outer surface of MCM-41 and Al-MCM-41 supports when the cobalt content was higher. On the other hand, by Transmission Electron Microscopy (TEM), it was possible to measure the interplanar distance of the crystalline plane of the outer nanoparticles, which was later compared with the theoretical distance values which allowed identifying the CoO and Co<sub>3</sub>O<sub>4</sub> phases.

© 2011 Elsevier Inc. All rights reserved.

### 1. Introduction

Metal and metal oxide nanoparticles have attracted increased attention due to their unusual physical and chemical properties. Moreover, it is well known that the nature, dispersion and size of the metal oxide particles are key factors in determining the activity and selectivity of the supported catalysts. These nanoparticles are typically loaded on porous supports, which prevent agglomeration and makes recovery easier. Some changes in the chemical nature of the support like acidity, basicity or redox properties, could be introduced to further tune the catalytic activity of the nanoparticles via metal–support interaction [1]. In this sense, the use of microporous and/or mesoporous materials as supports for metal and metal oxide nanoparticles offers several potential applications in fields such as catalysis, separation processes and nano-engineering [2–4]. Mesoporous silica MCM-41 is one of the most extensively studied meso-structure materials since it was first synthesized by Mobil Corporation in 1992 [5]. These materials were prepared through alkyltrimethylammonium cationic surfactant. The main

porous solids in the M41S family are called MCM-41, MCM-48 and MCM-50 (MCM: Mobil Crystalline Material).

Grün et al. [6] were pioneers in the synthesis of MCM-41 silicate with spherical morphology, which is of great interest due to their low density and high thermal and mechanical stability. These properties make these materials adequate as supports in catalytic reactions involving strong oxidizing conditions and extreme temperatures. The channel wall of MCM-41 essentially consists of amorphous SiO<sub>2</sub>. However, the neutral character of pure silica implies limitations of their applications in catalysis or adsorption. In this context, the incorporation of metal species is a straight way to provide the desired properties onto mesostructured samples. Thus, a variety of mesoporous materials was prepared using a diversity of procedures involving the incorporation of active species inside or on the silica walls. In this sense, the first metal whose incorporation started to be considered was aluminum. Today, numerous studies about the synthesis of Al-containing MCM-41 can be found in the literature [7,8]. One of the most widely employed synthesis methods is the co-condensation method which allows obtaining the Al atoms homogeneously dispersed in the SiO<sub>2</sub> matrix. In this vein, iron, cobalt or nickel substituted into MCM-41 silicates have proved to be active in catalytic reactions of oxidation [9]. Likewise,

\* Corresponding author. Tel./fax: +54 342 4536861.

E-mail address: [aboix@fiq.unl.edu.ar](mailto:aboix@fiq.unl.edu.ar) (A.V. Boix).

several publications on cobalt oxide particles supported on mesoporous materials have reported good catalytic performance in the total oxidation of toluene [10,11] and for the Fischer Tropsch reaction [12–14].

Recent research work has focused on new perspectives for the preparation of noble or transition metals or metal oxide nanoparticles into spherical MCM-41 [15,16]. Impregnation and grafting are the most usual post-synthesis methods but several authors have also used ion-exchange and chemical vapor deposition. A considerable amount of work has been published employing these techniques to load metals on the surface of mesoporous materials for a huge variety of catalytic applications. Incipient wetness impregnation is the most common technique employed to load metals on micro- and mesoporous materials. The principal advantage of this method is that it allows preparing materials with very high metal loading with many kinds of precursors. However, the dispersion degree achieved for the metallic sites is always low and decreases insofar the metal loading increases. Besides, the interaction existing between metal and support is usually weak since only the physisorption process can be achieved during the impregnation [17].

In addition, grafting is a method based on the reaction of the support surface hydroxyl groups ( $-\text{Si}-\text{O}-\text{H}$ ) with the metal precursor leading to covalent linkages between metal and silica surface ( $-\text{Si}-\text{O}-\text{Metal}$ ) [18]. One of the disadvantages is the preservation of the species and the possible interaction between the metallic sites and the uncovered silica surface. In the case of the incorporation of metallic cations on mesoporous materials by ion-exchange, it can be carried out in two ways: by exchanging acid positions of solids as Al-MCM-41 [19] or by exchanging template cations from as-synthesized MCM-41 materials [20–22]. The acid strength of Al-MCM-41 is not very strong compared with other materials such as zeolites and, therefore, metal-silica bonds generated through ion-exchange are usually labile. The second strategy, based on the exchange of templating cationic surfactants with metal species, is called the “template-ion exchange” (TIE) method. In this situation, template cations embraced in the channels of the as-synthesized solid are exchanged with the metal ions in solution [21]. The remaining template is removed by calcinations obtaining a porous and metal-functionalized mesoporous material. Since the TIE technique requires the use of ionic templates, they have been employed in the incorporation of metals to the MCM-41 material. In addition to these commonly employed methods, Supercritical Fluid Deposition (SCFD) is a promising method to deposit metallic nanoparticles and films on inorganic porous supports [23–26], polymer substrates [27] and carbon nanotubes [28]. Reactive supercritical deposition involves the dissolution of an organometallic precursor in a supercritical fluid (SCF), the impregnation of the substrate by exposure to this solution, and the subsequent decomposition/reduction of the precursor.  $\text{CO}_2$  is the most commonly used supercritical fluid ( $\text{scCO}_2$ ) for material synthesis because it is non-toxic, non-reactive, nonflammable and inexpensive [29]. Furthermore, residual  $\text{CO}_2$  is negligible in the processed product because of the gaseous character of  $\text{CO}_2$  at ambient conditions. Under supercritical conditions,  $\text{CO}_2$  as a solvent has intermediate properties between gases and liquids. The gas-like diffusivity and viscosity of  $\text{scCO}_2$  are favorable for rapid diffusion and permeation into mesoporous substrates whereas the liquid-like density allows the dissolution of a wide range of organometallic precursors. By means of small changes in P and/or T, it is possible to control the size, morphology and porosity of nanoparticles. The zero surface tension of  $\text{scCO}_2$  allows better penetration and wetting of pores than liquid solvents and avoids the pore collapse which can occur on certain structures. The simple removal from the substrate by controlled decompression is performed without leaving any residue on the support. In this sense, Crowley et al. [15] reported the synthesis of cobalt, copper and iron oxide nanowires

inside the pores of mesoporous silica using carbon dioxide ad supercritical fluid phase. Also, Hasell et al. [30] synthesized palladium nanoparticles throughout a microporous material by the reduction of organopalladium compounds dissolved in supercritical  $\text{CO}_2$ .

This work presents the synthesis of cobalt nanoparticles on MCM-41 and Al-MCM-41 supports in supercritical  $\text{CO}_2$ . The dispersion of cobalt species on both supports is discussed for two different cobalt loadings. The prepared samples were characterized by Scanning Electron Microscopy (SEM/EDX), Transmission Electron Microscopy (TEM), Small Angle X-ray Scattering (SAXS), Laser Raman Spectroscopy (LRS) and X-ray Photoelectron Spectroscopy (XPS).

## 2. Experimental

### 2.1. Synthesis of MCM-41 and Al-MCM-41

Mesoporous supports were synthesized in their spherical cshape as reported by Szègedi et al. [31]. 1 g of *n*-hexadecyltrimethylammonium bromide ( $\text{C}_{16}\text{TMABr}$ ) was dissolved in 19.2 g of de-ionized water and mixed with 24 g of absolute ethanol. 5.9 g of aqueous ammonia solution (29 wt.%) were added and stirred for 15 min. Under stirring, 1.88 g of tetraethylorthosilicate (TEOS) was added drop-wise in a couple of minutes. The resulting powder, with a molar composition of TEOS:  $0.3\text{C}_{16}\text{TMABr}$ :  $11\text{NH}_3$ :  $144\text{H}_2\text{O}$ :  $58\text{EtOH}$ , was stirred for 2 h and aged for additional 16 h at 25 °C. Aluminum containing MCM-41 with a Si/Al atio of 20 was prepared by introducing 0.04 g sodium aluminate into the reaction mixture before adding TEOS. The white precipitates were filtered and washed several times until neutral pH was reached. Then the samples were dried for 12 h at 60 °C. The template removal was carried out by heating the samples in air up to 600 °C at 1 °C  $\text{min}^{-1}$  heating rate.

### 2.2. Deposition of Co nanoparticles

Co/MCM-41 and Co/Al-MCM-41 samples were prepared by Supercritical Reactive Deposition. Cobalt nanoparticles were dispersed inside the mesoporous silica powder by the thermal decomposition of an appropriate organometallic precursor in  $\text{scCO}_2$ . Cobalt (II) bis-( $\eta^5$ -cyclopentadienil), also known as cobaltocene ( $\text{CoCp}_2$ ), was used as precursor because it is known to be highly soluble in  $\text{scCO}_2$  [32] and it has been utilized in the Co deposition of high purity thin films directly on silicon oxide [33].  $\text{CoCp}_2$  was obtained from Sigma Aldrich and used as received.  $\text{CO}_2$  (99.99%) was supplied by Carburros Metálicos (Spain). The mesoporous support was placed in the high-pressure reactor, 100 ml of internal volume, with no direct contact with the cobalt complex. At the beginning of each experiment, 100 mg of particulate support were placed in a glass tube of 15 mm diameter located inside the reactor, and the desired amount of organometallic precursor into a second glass tube of smaller diameter (6 mm). Both glass tubes were separated by a wire mesh to allow the entrance and circulation of  $\text{scCO}_2$ . In addition, the reactor was equipped with two wall electrical resistances and contained a K-Thermocouple to measure and control the reactor temperature. Both resistors were placed at the bottom of the reactor to promote convective flow of  $\text{scCO}_2$ . Deposition experiments were carried out in batch operation divided into two consecutive stages. During the first step, the dissolution of the  $\text{CoCp}_2$  precursor in  $\text{scCO}_2$  and the impregnation of the support occurred, and operational conditions were fixed at 70 °C and 110 bar during 3 h. The second step was the decomposition and deposition at 200 °C and 160 bar. After 3 h, the  $\text{scCO}_2$  was released from the reactor over a period of

approximately 1 h, which implied a slowly depressurization up to atmospheric pressure.

The cobalt loading was represented with 'x' in the Co(x)/MCM-41 and Co(x)/Al-MCM-41 samples and was determined by Inductively Coupled Plasma (ICP-OES).

### 2.3. Characterization techniques

#### 2.3.1. Scanning Electron Microscopy (SEM/EDX)

The application of SEM combined with detection by Energy Dispersive X-ray Spectroscopy (EDX) was performed to analyze the morphology of the support and to determine the chemical composition of the deposited particles.

An environmental scanning electron microscope (ESEM) FEI Quanta model 200FEG operating at 30 kV was used. Besides, a backscattered electron detector was used to observe the Co nanoparticles. This detector in particular was able to measure in Z-contrast, i.e. the contrast related to the atomic number ( $Z$ ) of the element upon which the beam impinges. Therefore, if there were phases with different  $Z$  of higher values, they would be brighter than the other phases.

The particle distribution analysis was achieved by means of digital mapping techniques in order to introduce the bi-dimensional spatial distribution of elements and to know the homogeneity of the cobalt inside the support. The X-ray mapping techniques from SEM/EDX analysis consisted in using pseudo-colors which represented the bidimensional spatial distributions of the energy emission of the sample chemical elements. Using this method, different colors were associated with diverse emission lines, whose width was equal to the energy channel resolution (20 eV in our case). In this way, it was possible to obtain one image for each emission energy with different contrast.

#### 2.3.2. Transmission Electron Microscopy (TEM)

A JEOL field emission microscope, model JEM-FS2200 HRP, operating at 200 kV was used. The samples were dissolved in methanol and were then placed in a carbon grid to be directly introduced into the microscope.

This technique was used to determine organization, morphology and pore dimension, as well as to observe the presence of metallic particles dispersed inside and/or outside the pores. In addition, this technique allowed measuring the nanoparticles interplanar distance.

#### 2.3.3. Nitrogen adsorption/desorption measurements

The surface area and pore size distribution were measured by means of a Micromeritics Accusorb 2100E instrument by the isotherms of adsorption and desorption of nitrogen at  $-196^\circ\text{C}$  on 200 mg of sample previously degassed at  $320^\circ\text{C}$  under high vacuum atmosphere for 8 h. Then, the materials were in contact with adequate amounts of nitrogen to cover the whole range of relative pressures close to saturation ( $p/p_0 = 0.995$ ).

#### 2.3.4. Small Angle X-ray Scattering (SAXS)

The MCM-41 diffractograms were easily identifiable because the arrangements of their channels only provided ( $h k 0$ ) reflections. Therefore, the X-ray diffraction patterns at low angle allowed assessing the degree of structural arrangement of the samples prepared.

The X-ray diffractions at low angle analysis were performed in a Hecus-Braun chamber which had a position-sensitive detector that allowed controlling the temperature of the sample. This equipment is installed on a PANalytical X-ray generation model PW3830. Measurements were made at  $2\theta$  between  $0^\circ$  and  $8^\circ$ .

#### 2.3.5. Laser Raman Spectroscopy (LSR)

The Raman spectra were recorded in a Horiba JOBIN YVON Lab RAM HR instrument. The excitation source was the 514.5 nm line of a Spectra 9000 Photometrics Ar ion laser with the laser power set at 30 mW. The powder sample was pressed at 4 bar into self-supporting wafers.

#### 2.3.6. X-ray Photoelectron Spectroscopy (XPS)

The XPS measurements were performed with the multitechnique system (SPECS) equipped with a dual X-ray source and hemispherical PHOIBOS 150 analyzer operating in the fixed analyzer transmission (FAT) mode. The spectra were obtained with pass energy of 30 eV and Al  $K\alpha$  radiation ( $h\nu = 1486.6$  eV) operated at 200 W and 12 kV. The working pressure in the analyzing chamber was less than  $5.9 \times 10^{-7}$  Pa. The spectra of Si 2p, Al 2p, Si 2s, Al 2s, C 1s, O 1s and Co 2p electronic level were recorded for each sample.

The data treatment was performed with the Casa XPS program (Casa Software Ltd., UK). The peak areas were determined by integration employing a Shirley-type background. Peaks were considered to be a mixture of Gaussian and Lorentzian functions in a 70/30 ratio. For the quantification of the elements, sensitivity factors provided by the manufacturer were used.

## 3. Results and discussion

### 3.1. Effect of operational parameters

In order to test the effect of pressure and temperature on mesoporous supports, calcined MCM-41 and Al-MCM-41 were located inside the high-pressure reactor at  $200^\circ\text{C}$  and 160 bar during 6 h since this was the total experimental time. No significant changes were observed in terms of  $A_{\text{BET}}$  and pore diameter, and TEM images of "fresh" and "CO<sub>2</sub>-treated" supports showed similar hexagonal patterns.

Experiments started at  $70^\circ\text{C}$  and 110 bar for a period of 3 h to guarantee dissolution of the CoCp<sub>2</sub> precursor in scCO<sub>2</sub> and impregnations of the support. High solubility, good mass transfer properties and good adsorption were desirable during this period. Adsorption was favored at low pressures, and CoCp<sub>2</sub> solubility in CO<sub>2</sub> increased with density, as was described by Aschenbrenner et al. [32]. Therefore, the operational conditions in this period were selected on the basis of obtaining good solubility at low pressures. According to the solubility values in the literature, the estimated solubility of CoCp<sub>2</sub> in CO<sub>2</sub> at  $70^\circ\text{C}$  and 110 bar is  $0.336\text{ g L}^{-1}$  [32]. Experiments were performed with two different initial amounts of precursor: 48 and 7 mg which corresponded to a maximum "theoretical" concentration in the supercritical phase of 0.48 and  $0.07\text{ g L}^{-1}$ , respectively. Therefore, in the first kind of experiments, the supercritical phase was saturated, and 14.4 mg of CoCp<sub>2</sub> remained in a solid state after the first 3 h, whereas in the other case, concentration was far below the solubility value, and the precursor located in the reactor was solubilized in the supercritical phase.

Thermal decomposition in the supercritical CO<sub>2</sub> phase took place at  $200^\circ\text{C}$  and 160 bar during 3 h. CoCp<sub>2</sub> was decomposed under these conditions as verified by comparing the IR spectra (not shown) of the precursor before and after 3 h under these conditions.

### 3.2. BET surface area and pore size distributions

Nitrogen adsorption and desorption experiments together with SAXS measurements were employed to study the effect of scCO<sub>2</sub> and the addition of cobalt on the surface area, mesoporous hexagonal arrangement and pore distribution of the prepared samples.

**Table 1**  
Textural properties of the prepared samples.

Samples	Co (wt.%) <sup>a</sup>	$A_{\text{BET}}$ ( $\text{m}^2 \text{g}^{-1}$ )	Pore size (nm)	$d_{100}$ <sup>b</sup>	$a_0$ <sup>c</sup>
MCM-41 calcined	0	1295	4.6	3.7	4.3
Co(0.6)/MCM-41	0.63	1183	4.5	3.7	4.3
Co(4.3)/MCM-41	4.34	1034	3.9	3.7	4.3
Al-MCM-41 calcined	0	807	4.8	3.7	4.3
Co(0.8)/Al-MCM-41	0.82	752	4.1	3.4	3.9
Co(5)/Al-MCM-41	5.10	709	3.9	3.4	3.9

<sup>a</sup> Determined by ICP.

<sup>b</sup> Interplanar distance, nm ( $d_{100} = \lambda/2 \cdot \sin \theta$ ).

<sup>c</sup> Unit cell parameter, nm ( $a_0 = 1.1547 \cdot d_{100}$ ).

Table 1 presents the results obtained by  $\text{N}_2$  adsorption-desorption measurements for the mesoporous supports, Co(x)/MCM-41 and Co(x)/Al-MCM-41 samples. The SAXS and ICP-OES results are also shown. All the solids gave typical type-IV isotherms (not shown) with a sharp inflection at relative pressure  $p/p_0 > 0.3$ , characteristic of capillary condensation, which indicates the uniformity of the mesoporous size distributions. It is noticeable that the addition of aluminum to the MCM-41 support produced a drop of approximately 38% in the  $A_{\text{BET}}$  while the pore size remained constant. In addition, from the same amount of precursor, the content of Co deposited on Al-MCM-41 was slightly higher compared to the support without aluminum. It is known that the addition of Al to pure silica is performed to give more acidity to the neutral character of the MCM-41 structure. Therefore, a mild interaction between aluminum and cobalt is likely to occur.

With the addition of 0.6 and 4.3 wt.% of Co to MCM-41 supports, a drop of 9% and 20% in the  $A_{\text{BET}}$  was observed, respectively. However, the area decreased by 7% and 12% for Co(0.8)/Al-MCM-41 and Co(5)/Al-MCM-41, respectively. Table 1 also summarizes the average pore size obtained from the BJH analysis of the prepared samples. The pore size slightly decreased with the increase of the cobalt loading added. This could be attributed to the addition of cobalt nanoparticles inside of the mesopores.

In this sense, to determine whether the addition of cobalt nanoparticles affected the channel arrangements of the mesoporous supports, the Small Angle X-ray Scattering (SAXS) technique was employed. It is usually applied to determine the presence of crystalline phases. In the case of amorphous materials such as MCM-41 and Al-MCM-41, the regular arrangement pores produce reflections that appear as signals at low diffraction angles. The M41S family samples have easily identifiable diffractograms due to their arrangement channels, providing only ( $h k 0$ ) reflections.

The results obtained by SAXS for the Co(x)/MCM-41 and Co(x)/Al-MCM-41 samples are shown in Fig. 1A and B, respectively. The appearance of a strong diffraction peak at  $2.4^\circ$  is characteristic of the (1 0 0) plane of the supports and indicates an ordered pore structure for MCM-41 and Al-MCM-41. The major intensity of this peak for the support without aluminum should be noticed. The weak diffraction peaks close to  $4.3^\circ$  and  $5.0^\circ$  which correspond to the (1 1 0) and (2 0 0) planes verify the synthesized mesoporous structure. This confirms that the synthesized spherical samples have a hexagonal arrangement.

The interplanar distance in the (1 0 0) direction, ' $d_{100}$ ', was calculated by Bragg's Law ( $\lambda = 2d_{hkl} \sin \theta$ ) and the unit cell parameter ' $a_0$ ' was also obtained, indicating the distance between the center of two adjacent pores in the hexagonal structure ( $a_0 = 2d_{100}/\sqrt{3}$ ) [31]. Both parameters are included in Table 1.

As shown in Fig. 1A, no distinct changes in the shapes and positions of the diffraction peaks can be observed at  $2\theta$  between 1 and 7 degrees for Co(x)/MCM-41 samples, indicating that the pore structure of MCM-41 remains unchanged after introducing the

Co atoms. The same behavior was observed on the Al-MCM-41 sample (Fig. 1B). However, with the addition of Co, there is a small shift of the main peak corresponding to the (1 0 0) plane to  $2.6^\circ$ , probably because the Co load produces a smooth loss of the hexagonal structure. The incorporation of cobalt into both supports decreases the intensity of the diffraction peaks, which indicates the disordering of the hexagonal arrangement of pores [34].

In the wide-angle XRD pattern (not shown) of Co(x)/MCM-41 and Co(x)/Al-MCM-41, there are no characteristic diffraction peaks of cobalt oxide or metallic cobalt, which indicates that cobalt species are well dispersed in the support and that, probably, the size of the nanoparticles is below 4 nm, which is the detection limit for the crystalline domain to be observed by XRD.

TEM and X-ray mapping from SEM images techniques are required to determine whether the metal is deposited on the porous structure or externally on the surface of the mesoporous support.

### 3.3. Characterization of the cobalt nanoparticles deposited

The SEM images in Fig. 2 show that the morphologies of synthesized MCM-41 (Fig. 2A) and Al-MCM-41 (Fig. 2B) meso-materials are spherical and the mean size is around 500 nm. The temperature and surfactant concentration used during the synthesis process are factors which affect the shape of the prepared samples. Thus, when the template concentration is between the critical micelle concentration (CMC, 0.1 wt.% relative to water at  $25^\circ\text{C}$ ) and 2 wt.%, the spherical micelles can be formed, while the rod-shaped micelles can be obtained when the surfactant concentration is greater than 2 wt.% [35]. In this work, the  $\text{C}_{16}\text{TMABr}$  is 1.92 wt.%; thus, the inorganic-organic silicate spherical micelles will be formed in the synthesis process and then, the aggregation of spherical micelles by self-assembly results in the formation of the final spherical MCM-41 and Al-MCM-41 particles. After the Co addition by supercritical  $\text{CO}_2$ , the spherical morphology of the mesoporous particles is remained (not shown). Individual nanoparticles cannot be directly observed using the secondary electron mode of the SEM. However, when the imaging is performed using the backscattered electron (BSE) mode, the presence of high electron dense areas, i.e. metallic particles, can be inferred. When it is coupled with EDX, approximate cobalt quantifications are possible. Fig. 3A and B shows the BSE images obtained from the Co(5)/Al-MCM-41 and Co(4.3)/MCM-41 samples, respectively. In the BSE image bright patches are observed, which indicate high electron dense areas, where increased brightness is due to the presence of a metal. The areas of high electron density appear well dispersed and correspond to cobalt nanoparticles with approximately 20 nm of diameter.

The EDX results from the SEM field of view in Fig. 3 return a cobalt loading of 5.9 and 5.1 wt.% for Co(4.3)/MCM-41 and Co(5)/Al-MCM-4, respectively. These EDX data should be interpreted with caution since this technique is highly selective because the metal loading is detected from one field of view only. However, it is useful to confirm the presence of cobalt nanoparticles with concentration values similar to those predicted by ICP-OES analysis (close to 5 wt.%).

Figs. 4 and 5 show the X-ray mapping results in SEM images obtained for Co(0.6)/MCM-41 and Co(4.3)/MCM-41, respectively. Different colors in grayscale are associated with diverse emission lines. In this way, each color in the picture refers to the single emission energy of the interesting element. When the Co loading is 0.6 wt.%, a homogeneous distribution of different cobalt species in mesoporous spheres is observed. However, when the cobalt content increases to 4.3 wt.%, spherical nanoparticles on the outer surface of MCM-41 support are observed. The diameter of these nanoparticles varies between 10 and 15 nm. As previously mentioned, for a Co content of 4.3 wt.%, the initial amount of  $\text{CoCp}_2$

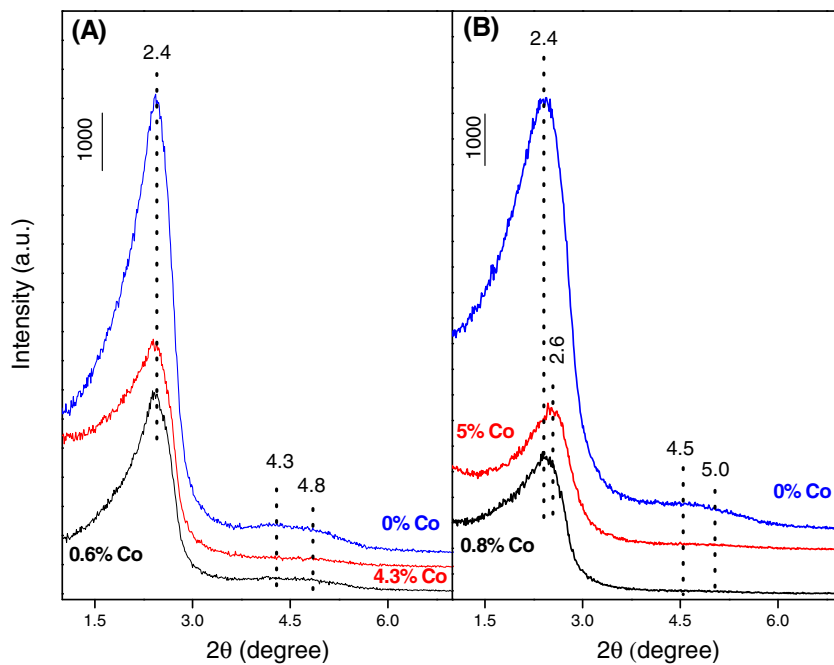


Fig. 1. SAXS results for: (A) Co(x)/MCM-41 and (B) Co(x)/Al-MCM-41.

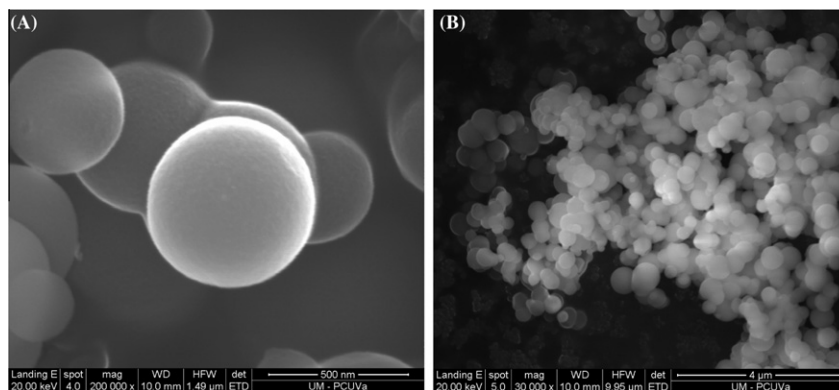


Fig. 2. SEM images of calcined (A) MCM-41 and (B) Al-MCM-41.

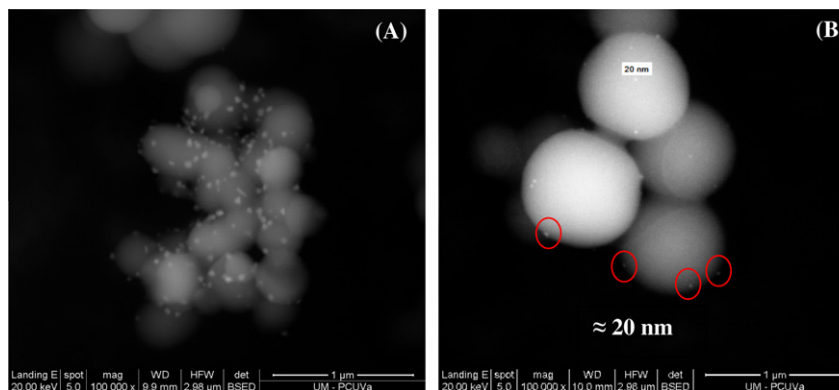


Fig. 3. BSE SEM images of (A) Co(5)/Al-MCM-41 and (B) Co(4.3)/MCM-41.

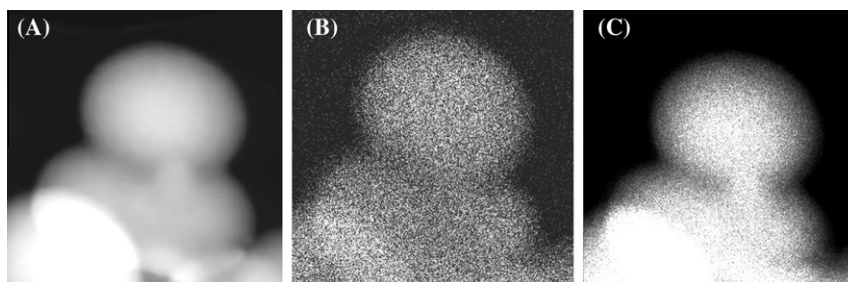


Fig. 4. X-ray SEM/EDX mapping for Co(0.6)/MCM-41; (A) electron image, (B) Co K $\alpha$  and (C) Si K $\alpha$ .

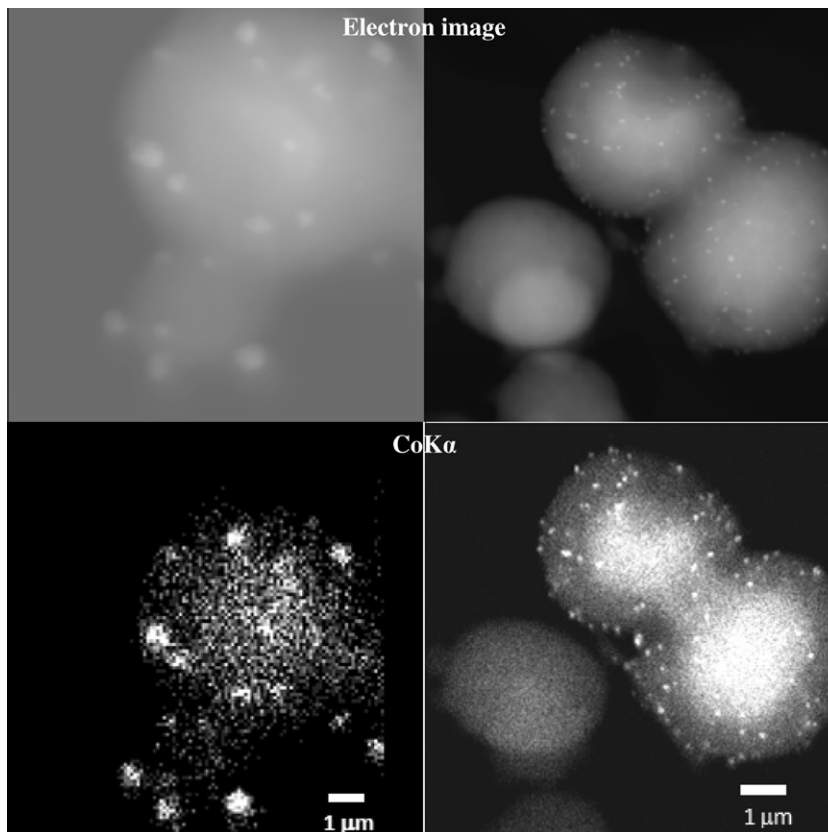


Fig. 5. X-ray SEM/EDX mapping for Co(4.3)/MCM-41.

located in the reactor is higher than the solubility value, and the solid precursor remains without dissolution after the dissolution and impregnation stage. Therefore, during the decomposition stage, the deposition of cobalt nanoparticles also takes place on the outer surface.

From these results, it can be observed that with a low Co loading on both supports, the nanoparticles locate inside the mesoporous spheres. When the cobalt load increases and the initial concentration is higher than the solubility value in the supercritical phase, the nanoparticles can be observed both inside the spheres and also on the surface of the MCM-41 and Al-MCM-41 supports.

In order to corroborate the outer nanoparticle sizes obtained from SEM and to differentiate the cobalt species, TEM analysis was employed. Fig. 6A shows a TEM image of MCM-41 mesoporous silica powder. The image displays a hexagonal array of mesopores with a pore diameter close to 5 nm, which is in agreement with the BJH results. With the addition of small amounts of aluminum

(Si/Al = 20) no significant differences in the size of the mesopores (Fig. 6B) were observed.

Fig. 7 shows the TEM images of cobalt deposited on the mesoporous support. The image of the amorphous MCM-41 and Al-MCM-41 samples is fuzzy while some cobalt nanoparticles can also be observed on the surface. These nanoparticles appear as dark spheres close to 20 nm in diameter. Likewise, the TEM micrographs of the Co(5)/Al-MCM-41 sample (Fig. 8) show the presence of Co nanoparticles on the surface, with diameters between 15 and 20 nm. Moreover, the interplanar distances of the nanoparticles can be measured and compared to their theoretical values (Table 2). It was found that the lattice spacing of 0.20 nm (Fig. 8A) possibly corresponds to the (2 0 0) plane belonging to CoO phase. Likewise, this distance is coincident with the crystallographic (1 1 1) plane of metallic cobalt. Crystallographic planes belonging to Co<sub>3</sub>O<sub>4</sub> were also found at 0.26, 0.24 and 0.26 nm, which can be assigned to the (4 4 0), (3 1 1) and (2 2 0) planes, respectively (Fig. 8B) [36].

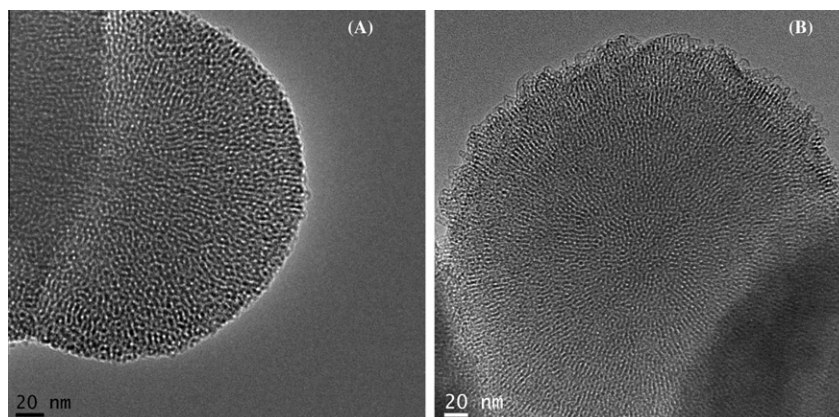


Fig. 6. TEM images of calcined (A) MCM-41 and (B) Al-MCM-41 samples.

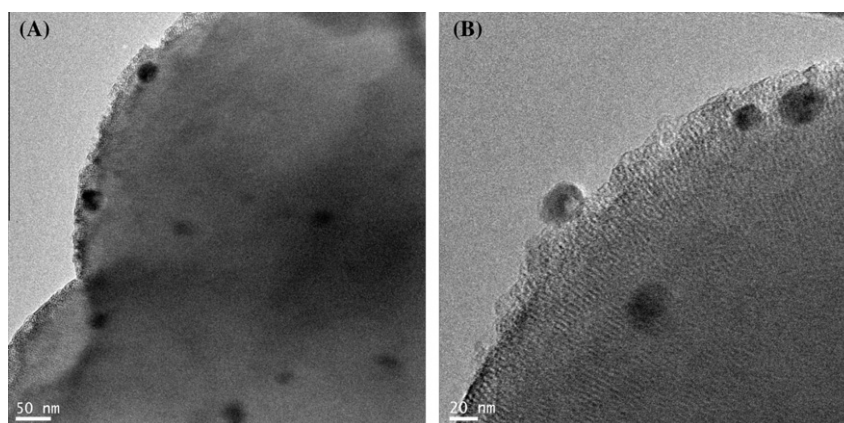


Fig. 7. TEM images of (A) Co(4.3)/MCM-41 and (B) Co(5)/Al-MCM-41 samples.

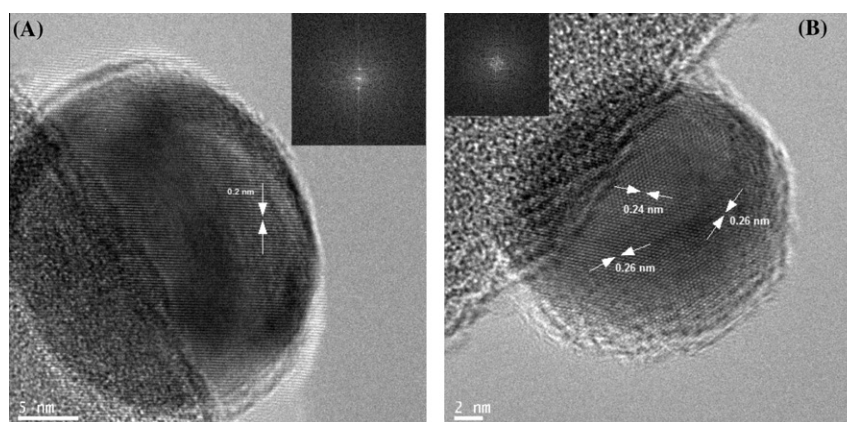


Fig. 8. TEM images of Co(5)/Al-MCM-41 sample with a magnification of (A) 500000 $\times$  and (B) 600000 $\times$ .

The presence of  $\text{Co}_3\text{O}_4$  nanoparticles on  $\text{Co}(x)/\text{Al-MCM}41$  could be determined by Raman spectroscopy. Fig. 9 presents the Raman spectra of the  $\text{Co}(x)/\text{MCM-41}$  and  $\text{Co}(x)/\text{Al-MCM-41}$  samples. The spectra of the samples with lower cobalt loading,  $\text{Co}(0.6)/\text{MCM-41}$  and  $\text{Co}(0.8)/\text{Al-MCM-41}$ , present several bands at 495, 602, 818 and  $973\text{ cm}^{-1}$  corresponding to the mesoporous supports. In addition, a small signal appears at  $690\text{ cm}^{-1}$ . At higher cobalt loading (spectra (b) and (d)), the intensity at  $690\text{ cm}^{-1}$  increases and a new signal appears at  $520\text{ cm}^{-1}$ . Both signals correspond to the main bands of the  $\text{Co}_3\text{O}_4$  spinel phase [37]. Due to the stability of the  $\text{CO}_2$  molecule, the oxidation of cobalt species to  $\text{Co}_3\text{O}_4$  should

be attributed to the traces of  $\text{O}_2$  present in the solvent. In all the experiments, commercial  $\text{CO}_2$  (>99.99% purity grade) was used, and its  $\text{O}_2$  content was  $10\text{ mg L}^{-1}$  STP. This value assumes an amount of ca.  $150\text{ mg O}_2$  in the reactor, enough to oxidize the  $\text{Co}^{2+}$  of the precursor to  $\text{Co}_3\text{O}_4$ . Due to the presence of oxygen traces, the oxidating character of commercial  $\text{CO}_2$  has been discussed elsewhere for unsaturated products [38].

These results can be supplemented with the chemical analysis of the substrate surface. The XPS technique was used to determine the oxidation state of Co nanoparticles in the prepared samples. The binding energy (BE) values of the  $\text{Co } 2p_{3/2}$  core-level are close to

**Table 2**  
Theoretical values of interplanar distance ( $d$ ) for cobalt species.

Species	Plane	$d^a$ (nm)
Co <sub>3</sub> O <sub>4</sub>	311	0.24
	440	0.24
	220	0.28
CoO	200	0.21
	111	0.24
	220	0.15
Co <sup>o</sup>	111	0.21

<sup>a</sup> Theoretical interplanar distance (Å),  $d = 2/\lambda \sin(\theta)$ .

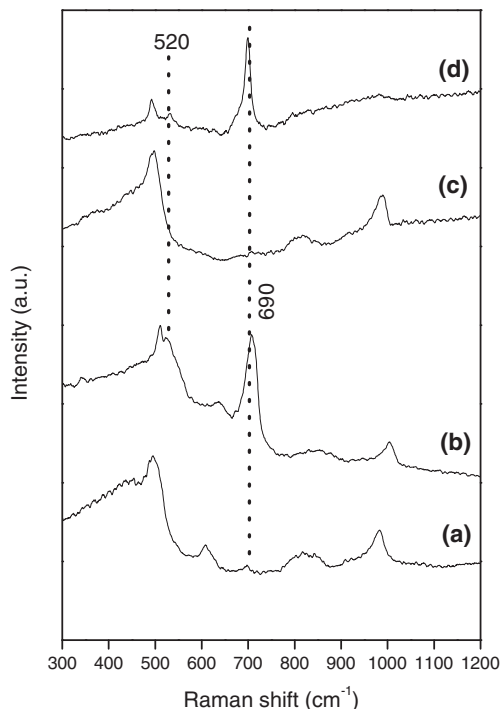


**Fig. 9.** Raman spectra of (a) Co(0.8)/Al-MCM-41, (b) Co(5)/Al-MCM-41, (c) Co(0.6)/MCM-41 and (d) Co(4.3)/MCM-41 samples.

782.0 eV for Co<sup>2+</sup> at exchange position on Co-zeolites and the BE at 780.0 eV for Co<sup>2+</sup> on CoOx [37]. The main peak is accompanied by a relatively intense 3d → 4s shake-up satellite peak at 787.5 eV characteristic of Co<sup>2+</sup> species. Spin-orbital splitting upon ionization between 2p<sub>3/2</sub> and 2p<sub>1/2</sub> is 16 eV [39]. XPS spectra of the synthesized materials in the Co 2p region are shown in Fig. 10. The BE of Co 2p<sub>3/2</sub> peak is ca. 781.2 eV and the shake-up satellite peak at 786.4 eV. These binding energies correspond to cobalt oxide species highly dispersed with a strong interaction with the structure. This fact produces a shift to higher BE values of 1.1 eV compared to the BE of Co 2p<sub>3/2</sub> on massive Co<sub>3</sub>O<sub>4</sub> or CoO (~780.2 eV). The decrease in intensity of the Co 2p region for the samples with a lower Co content (Fig. 10, spectra a and b) is possible due to the lower concentration of Co species and probably, the oxide phase is finely dispersed inside the support structure in agreement with the TEM images. The binding energies of Si 2p and Al 2p core-level spectra for all samples were 103.4 and 74.1 eV, respectively, in agreement with Jalil et al. [40].

#### 4. Conclusions

Supercritical CO<sub>2</sub> is a suitable, simple and effective medium to incorporate cobalt nanoparticles on mesoporous MCM-41 and Al-MCM-41 materials. Cobalt oxide nanoparticles were uniformly

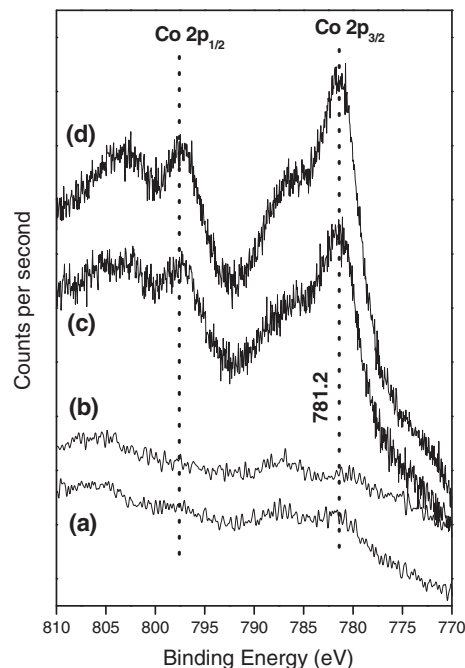


**Fig. 10.** Co 2p XPS spectra of (a) Co(0.6)/MCM-41, (b) Co(0.8)/Al-MCM-41, (c) Co(4.3)/Al-MCM-41 and (d) Co(5)/Al-MCM-41 samples.

dispersed in Al-free and Al-containing supports. The experimental results show that it is important to control the initial precursor concentration during the first synthesis stage. This value should be lower than the solubility limit in order to prevent particle growth on the outer surface. Moreover, the presence of aluminum in the Al-MCM-41 support allowed the incorporation of a higher concentration of cobalt compared to the Al-free support.

TEM, Laser Raman and XPS indicated the presence of well-dispersed CoO and Co<sub>3</sub>O<sub>4</sub> nanoparticles inside both substrates, with an average size of less than 4 nm. When the cobalt content was close to 5%, “extra” nanoparticles 10–20 nm in size appeared on their outer surface. This is because the initial amount of the precursor was higher than the solubility value with scCO<sub>2</sub>. No significant changes were observed in the hexagonal arrangement and specific surface area of mesoporous supports after adding a high content of cobalt nanoparticles (close to 5 wt.%).

#### Acknowledgements

The authors acknowledge the financial support received from Junta de Castilla y León, Spain, (JCYL Ref.: GR11) and from Universidad Nacional del Litoral and CONICET, Argentina. They are also grateful to ANPCyT (Argentina) for the purchase of the SPECS multitechnique analysis instrument (PME8 -2003) and the Laser Raman Spectrometer (PME Grant 36 985 87-PAE). Thanks are given to Prof. Elsa Grimaldi for the English language editing.

S.A. thanks the ERASMUS MUNDUS – EADIC Lot. 16 Program, coordinated by Bologna University and financed by the European Community.

#### References

- [1] J. Garcia-Martinez, N. Linares, S. Sinibaldi, E. Coronado, A. Ribera, *Micropor. Mesopor. Mater.* 117 (2009) 170–177.
- [2] W. Wang, Y. Li, R. Zhang, D. He, H. Liu, S. Liao, *Catal. Commun.* 12 (2011) 875–879.
- [3] S. Todorova, V. Pãrvulescu, G. Kadinov, K. Tenchev, S. Somacescu, B.L. Su, *Micropor. Mesopor. Mater.* 113 (2008) 22–30.
- [4] Y. Xia, H. Dai, H. Jiang, L. Zhang, *Catal. Commun.* 11 (2010) 1171–1175.

- [5] C.T. Kresge, M.E. Leonowicz, W.J. Roth, J.S. Beck, *Nature* 359 (1992) 710–712.
- [6] M. Grün, K.K. Unger, A. Matsumoto, K. Tsutsumi, *Micropor. Mesopor. Mater.* 27 (1999) 207–216.
- [7] M.V. Landau, E. Dafa, M.L. Kaliya, T. Sen, M. Herskowitz, *Micropor. Mesopor. Mater.* 49 (2001) 65–81.
- [8] X.S. Zhao, G.Q. Lu, G.J. Millar, *Ind. Eng. Chem. Res.* 35 (1996) 2075–2090.
- [9] V. Parvulescu, B.L. Su, *Catal. Today* 69 (2001) 315–322.
- [10] A. Szegedi, M. Popova, A. Dimitrova, Z. Cherkezova-Zheleva, I. Mitov, *Micropor. Mesopor. Mater.* 136 (2010) 106–114.
- [11] Á. Szegedi, M. Popova, C. Minchev, *J. Mater. Sci.* 44 (2009) 6710–6716.
- [12] I.T. Ghampton, C. Newman, L. Kong, E. Pier, K.D. Hurley, R.A. Pollock, B.R. Walsh, B. Goundie, J. Wright, M.C. Wheeler, R.W. Meulenberg, W.J. DeSisto, B.J. Frederick, R.N. Austin, *Appl. Catal. A: Gen.* 388 (2010) 57–67.
- [13] B.V. de Sousa, M.G.F. Rodrigues, L.A. Cano, M.V. Cagnoli, J.F. Bengoa, S.G. Marchetti, G. Pecchi, *Catal. Today* (2011), doi:10.1016/j.cattod.2011.02.035.
- [14] O. González, H. Pérez, P. Navarro, L.C. Almeida, J.G. Pacheco, M. Montes, *Catal. Today* 148 (2009) 140–147.
- [15] T.A. Crowley, K.J. Ziegler, D.M. Lyons, D. Erts, H. Olin, M.A. Morris, J.D. Holmes, *Chem. Mater.* 15 (2003) 3518–3522.
- [16] Y. Wang, Y. Ohishi, T. Shishido, Q. Zhang, W. Yang, Q. Guo, H. Wan, K. Takehira, *J. Catal.* 220 (2003) 347–357.
- [17] J.A. Schwarz, C. Contescu, A. Contescu, *Chem. Rev.* 95 (1995) 477–510.
- [18] N. Brusnel, P. Bellocq, A. Sutra, M. Cauvel, P. Lasperas, F. Moreau, *Coord. Chem. Rev.* 178–180 (1998) 1085–1108.
- [19] G.V. Shanbhag, T. Joseph, S.B. Halligudi, *J. Catal.* 250 (2007) 274–282.
- [20] M. Yonemitsu, Y. Tanaka, M. Iwamoto, *Chem. Mater.* 9 (1997) 2679–2681.
- [21] Q. Zhang, Y. Wang, S. Itsuki, T. Shishido, K. Takehira, *J. Mol. Catal. A: Chem.* 188 (2002) 189–200.
- [22] D. Marczewska, W. Gac, N. Popivnyak, G. Zukozinski, S. Pasoeczna, *Catal. Today* 114 (2006) 293–306.
- [23] C. Erkey, *J. Supercrit. Fluids* 47 (2009) 517–522.
- [24] D.P. Long, J.M. Blackburn, J.J. Watkins, *Adv. Mater.* 12 (2000) 913–915.
- [25] K.S. Morley, P.C. Marr, P.B. Webb, A.R. Berry, F.J. Allison, G. Moldovan, P.D. Brown, S.M. Howdle, *J. Mater. Chem.* 12 (2002) 1898–1905.
- [26] J.M. Blackburn, D.P. Long, A. Cabañas, J.J. Watkins, *Science* 294 (2001) 141–145.
- [27] J. Yang, T. Hasell, D.C. Smith, S.M. Howdle, *J. Mater. Chem.* 19 (2009) 8560–8570.
- [28] X.Y. Lin, C. Wang, M.H. Engelhard, Y. Wang, C.M. Wai, *J. Mater. Chem.* 14 (2004) 908–913.
- [29] E. Reverchon, R. Adami, *J. Supercrit. Fluids* 37 (2006) 1–22.
- [30] T. Hasell, C.D. Wood, R. Clowes, J.T.A. Jones, Y.Z. Khimyak, D.J. Adams, A.I. Cooper, *Chem. Mater.* 22 (2010) 557–564.
- [31] A. Szegedi, Z. Kónya, D. Méhn, E. Solymár, G. Pál-Borbély, Z.E. Horváth, L.P. Biró, I. Kiricsi, *Appl. Catal. A: Gen.* 272 (2004) 257–266.
- [32] O. Aschenbrenner, S. Kemper, N. Dahmen, K. Schaber, E. Dinjus, *J. Supercrit. Fluids* 41 (2007) 179–186.
- [33] E.T. Hunde, J.J. Watkins, *Chem. Mater.* 16 (2004) 498–503.
- [34] I. Sobczak, M. Ziolk, M. Nowacka, *Micropor. Mesopor. Mater.* 78 (2005) 103–116.
- [35] H. Liu, G. Lu, Y. Guo, Y. Wang, Y. Guo, *J. Colloid Interf. Sci.* 346 (2010) 486–493.
- [36] S. Sun, Q. Gao, H. Wang, J. Zhu, H. Guo, *Appl. Catal. B: Environ.* 97 (2010) 284–291.
- [37] A.V. Boix, S.G. Aspromonte, E.E. Miró, *Appl. Catal. A: Gen.* 341 (2008) 26–34.
- [38] M.J. Cocero, S. González, S. Pérez, E. Alonso, *J. Supercrit. Fluids* 19 (2000) 39–44.
- [39] A. Boix, J.L.G. Fierro, *Surf. Interf. Anal.* 27 (1999) 1107–1113.
- [40] P.A. Jalil, M.S. Kariapper, M. Faiz, N. Tabet, N.M. Hamdan, J. Diaz, Z. Hussain, *Appl. Catal. A: Gen.* 290 (2005) 159–165.